COMPREHENSIVE INTEGRATED ANATOMICAL AND MOLECULAR ATLAS OF RODENT INTRINSIC CARDIAC NERVOUS SYSTEM

Achanta Sirisha[1], Gorky Jonathan[1], Leung Clara[2], Moss Alison[1], Robbins Shaina[1], Eisenman Leonard[1], Chen Jin[2], Tappan Susan[3], Maci Heal[3], Farahani Navid[4], Huffman Todd[4], Cheng Zixi[2], Vadigepalli Rajanikanth[1], Schwaber James[1]

ABSTRACT

In recent years neuroanatomy research of mammalian brain has come to the forefront through the development of three-dimensional (3D) digital reference atlases at cellular scale, and the revelation of the complex diversity of the molecular phenotypes of neurons, often with orderly spatial gradients of neuron types. This report builds on these approaches and brings them to bear on rodent intrinsic cardiac nervous system (ICN). We present a comprehensive 3D mapping of rat ICN in the overall histological and ontological context of the heart and demonstrating anatomically specific single-neuron transcriptional gradients. The development of the approaches needed to acquire these data have produced methods pipelines which can achieve the goals of the NIH Directors Initiative Stimulating Peripheral Activity to Relieve Conditions (SPARC): Comprehensive Functional Mapping of Neuroanatomy of the Heart. We herein show the development, coordination, and integration of several technologies including novel whole organ imaging, software development, precise 3D neuroanatomical mapping and molecular phenotyping into a robust pipeline that can achieve the SPARC goal of a comprehensive foundational data resource.

INTRODUCTION

Autonomic control of cardiac function contains several integrative centers in the central nervous system, including the dorsal vagal complex, nucleus ambiguus, ventrolateral medulla, and the intermediolateral cell columns of the spinal cord. However, the final level of neural integration controlling cardiac function lies in the ICN. While the heart is known to possess a significant population of neurons, these have not previously been mapped as to their number, extent/position/distribution while maintaining the histological context of the heart. This 3D neuroanatomical information is necessary to understand the functional connectivity of the neurons and to develop their functional circuit organization. Mapping of molecular phenotypes and cell functions must also occur in the anatomical context to ensure a holistic comprehension of the system.

While qualitative and gross anatomical descriptions of the anatomy of the ICN have been presented, we here bring forth the first comprehensive atlas of the cardiac ICN in rat at a cellular level. This work represents the next logical steps in a long history of attempts to understand the anatomical substrate upon which the neuronal control of

cardiac function is built. There has not yet been a comprehensive effort to generate a neurocardiac atlas for any species, nor any effort to generate a histological mapping at the single neuron level for the whole heart of any species.

Prior mapping efforts of ICN in small animals have included: mouse (Li et al., 2010, 2014; Rysevaite et al., 2011a), rat (Ai et al., 2007; Cheng et al., 2004, 1999; Cheng and Powley, 2000), rabbit (Saburkina et al., 2014), guinea pig (Hardwick et al., 2014; Steele et al., 1994). With these efforts, there was either restricted anatomical regions that were mapped at a microscopic level or large gross anatomical regions that were not mapped microscopically. While qualitative and gross anatomical descriptions of the anatomy of the ICN have been presented, we present the first comprehensive atlas of the cardiac ICN in rat at a cellular level.

We here developed and apply a methods pipeline to create a comprehensive mapping, within the 3D structure of the heart, of cardiac neurons in a male and female rat heart. These integrative datasets are informative and useful in their own right as a first appreciation of the rodent ICN and of single-neuron transcriptional profiling in this population. We combined a diverse set of technologies that enabled a geographically distributed network of researchers to coordinate and offer distinct skills enabling the present results. These are graphically represented in the two data pipelines in Figure 1. In the pipeline represented in Figure 1A we used the 3Scan histological scanning technology in order to make an accurate and comprehensive 3D reference framework of the neuroanatomy of the heart. In parallel we developed software tools for mapping the ICN in context of the whole heart. We took these images to MBF Bioscience group with expertise in 3D model building to develop the TissueMaker and TissueMapper software tools for mapping neurons in peripheral organs. The former imports section images, aligns, orders and stacks the images into an image volume, and supports graphic manipulations of each image as needed. The output from this are xml and jpx files for TissueMapper to mark, map and store histological, cellular and structural features visible in the tissue section. These are described in detail in the Methods and Supplement. Then, collaborators at UCF and TJU brought skills to bear on anatomical mapping at the heart and single-cell transcriptomics in anatomical context. Alternatively, the pipeline in Figure 1B uses cryostat sectioning of the heart that permits acquisition of neurons as single cell scale samples with the ability to ascertain circuit connectivity and molecular phenotypes. Then the molecular phenotype(s) of these neurons can be placed in whole heart and ICN context. Images of these sections, including neuronal positions, are stacked to create a whole heart volume with neuronal phenotype data that can be brought into the 3D reference systems created by the first approach. See the Methods section below for details.

RESULTS

Comprehensive Neuroanatomy of the Rat Heart

The above combined network of capabilities has enabled a comprehensive representation of the rat ICN at the level of detailed cellular histology in context of the whole heart as an accurate 3D model of the organ. The position of neurons and contours of major anatomical cardiac features were mapped from histological section images acquired by the pipeline described in Figure 1A. Having the 3D graphics model of the comprehensive ICN we used supervised visual analysis to describe the ICN in several ways. We use the standard anatomical planes to provide familiar points of view and we emphasize a posterior view and a superior view of the heart and ICN.

- We visualize the ICN in the context of the 3D graphical model of the whole heart. We visualize and describe the extent, distribution and location of ICN neurons in the anterior-posterior (dorsal-ventral) and transverse or axial-median dimensions. Figures 2 and 3 show the ICN distribution in the context of the whole heart from a standard posterior point of view. This shows the extensive distribution on both the posterior atria extending in the superior-inferior dimension. Figure 3 is a slab from the middle of the distribution created using the Partial Projection tool in the TissueMapper software.
- The ICN literature typically emphasizes the localization of neurons to the hilum, around the major vessels. We also aimed to better understand the left-right atrium neuronal distribution. To this end we use the standard superior anatomic plane in Figure 4 and 5. Figure 4B illustrates on a transverse slab the position of neurons on the base of the heart at the hilum. Figure 5 is also a restricted transverse slab made by Partial Projection but viewing only the more inferiorly (caudally) located neurons.
- We describe the position of ICN neurons in histological sections. Figure 6 consists of single sagittal section views of the ICN across the superior-inferior axis. Figure 7 moves from qualitative to illustrations reflecting quantitative analyses of neuron distributions and packing density. Figure 8 shows the ICN in the digitized high-resolution images of histological sections. Figures 8 & 9 illustrate the strategy used in which we employed the pipeline represented in Figure 1B, to capture single neurons for molecular analysis. Figure 10 visualizes the mapped ICN distribution to the distribution of samples taken and analyzed for molecular phenotypes. Figures 11-13 present analyses of molecular neuronal phenotypes, and demonstrate the gradients and distribution of phenotypes across the extent of the ICN.

The results from these visual and quantitative analyses are discussed below.

We sought to delineate the distribution, extent and location of neurons on the heart in part by use of 3D graphical models of the ICN in cardiac context both in figures and by rotating the model in a movie available at this link:
https://mbfbioscience.sharefile.com/d-sa1501de2ad94d3f9

Rotating the 3D model framework of the ICN allows points of view that display the distribution and position of ICN neurons on the posterior surface of the atria as they extend into the coronary sulcus or groove that separates the atria and ventricles. Figure 2A shows the standard posterior plane point of view, in which the entire population can be seen to be compact and localized to a regionally localized region on the superior and posterior aspects of the atria, extending inferiorly to the boundary with the ventricle. . Figure 2B-F are enlarged images of the region of the heart in the dotted yellow box of Figure 2A This provides a better appreciation the ICN distribution, shape and location in relation to cardiac structures. This allows the position and extent of the ICN to be seen in the context of various structures. In Figure 2B the zoomed-in ICN appears to comprise three or more large clusters in which neurons extend rostrally to caudally as a tortuous but almost continuous column-like neuronal population as multiple ganglionated plexuses. Figure 2C shows that the ICN lies several mm lateral to the aorta, adjacent and posterior to the aorta. Figure 2D shows the ICN relative to the interatrial septum. In this view, there is a population of neurons that appear to be mostly located on the posterior surface of the left atrium. There is also a group of (neurons located within the interatrial septum and on the right atrium. This again shows the ICN is associated with or within the posterior wall of both the left and right atria as well as the interatrial septum. In 2E the ICN is displayed in relation to the contours of the left atrium and in 2F to the contours of the right atrium. The most prominent columns of neurons are positioned on the left atrium and/or across both atria. There are three large clusters of ICN observed with respect to the right atrium denoted as #1, #2, and #3. Clusters #1 and #2 appear to be on the epicardial surface of both atria, while cluster #3, located adjacent to the borders of the superior vena cava, left atrium, and right atrium, appears to be partially within the right atrium.

The ICN distributes on the posterior atria. In order to position these neurons in higher resolution of just posterior cardiac structures we used the “virtual section” Partial Projection tool from the TissueMapper software. Figure 3 shows a 3 mm slab oriented superior-inferior, centered on the posterior cardiac surface. This shows a more restricted portion of the structure while presenting a more coherent view than single sections can provide. At these levels the majority of neurons appear inferior-caudal to the base of the heart, extending to the coronary sulcus. This slab and point of view is focused on the posterior surface of the heart. This has the advantage of providing a broader context than single sections but also a more focused examination than the full

3D heart context. In Figure 3 this partial projection of the ICN is a localized, compact population of neuronal clusters with a superior-inferior orientation, distributed on both atria and in the IAS, but preferentially to the left atrium.

By rotating the 3D model, we found that a superior view, i.e. looking down at the base of the heart, provided the ability to distinguish neurons associated with the right vs. the left atrium. Figure 4A takes a standard superior view of the 3D heart and ICN, viewing the base of the heart. The distribution of all ICN neurons can be seen in the context of the major vessels on the base of the heart. In particular the left atrium and right atrium distribution of neurons can be observed in relation to the interatrial septum (IAS), with neurons associated with both atria, but more so to the left atrium, with a smaller population within the IAS itself. In Figure 4A, the entire population of the ICN is seen from a superior viewpoint allowing appreciation of the full distribution of neurons on the left and right atria.

Since in rat the ICN are often associated with the hilum on the base of the heart we want to examine only neurons with that specific neuroanatomical distribution and localization. In Figure 4B' and 4B we aim to acquire and then only visualize neurons plausibly located on the base of the heart. Using the "Partial Projection" tool it is possible to take an intermediate slab of the of the 3D heart model and neurons in any plane and thickness, more than single sections and less than the full 3D model. Using this tool we made a virtual section that visualizes only neurons at the superior (cranial) end of the ICN located at the base of the heart. Then, in Figure 4B these neurons are seen in the context of the base in a superior view of the heart. These ICN neurons are on the epicardial aspect of the base associated with the major pulmonary vessels there, the cardiac hilum. These neurons appear to be on the right atrium and in the interatrial septum.

Our results show that the majority of neurons are positioned more inferiorly to the base of the heart extending caudally to the boundary with the ventricles as seen in Figures 2&3. In order to visualize their distribution and location across the two atria we again took a superior view of the heart to observe left-right neuronal distribution of neurons, but used the TissueMapper software "Partial Projection" tool to "cut off the base/hilum) and observe only neurons inferior to the base of the heart (Figure 5). This graphic shows those ICN neurons as a transverse or axial visualization of a 3 mm thick slab of tissue. Neuron clusters are abundant across both atria, but in contrast to the base of the heart neurons are more abundant on the left atrium.

The 3D reference models of the heart and ICN are derived from whole-mount stained histological tissues (i.e. whole rodent hearts). It is also informative to look at these

single tissue sections and appreciate the position of the neurons in them. The “native” section images in Figure 6 are from the data acquisition pipeline in Figure 1A. These six 5um tissue section images are at 0.5um resolution and allow appreciation of the cellular histology for discriminating neurons. As such, individual neurons could be identified and their locations determined in relation to the heart chambers and other structures, as shown at six different levels of the heart (Figure 6). This heart was sectioned in a near-sagittal plane and Figure 6A-F moves sequentially from the right to the left side of the heart. The full image stack of all the sections are available through the Supplement. Figure 6A is close to the right side limit to the ICN and 6F the left limit. The numbers in each panel indicate the right-left position of the section. Thus, Figure 6A is1285 microns from the right heart edge and Figure 6F is be 4020 microns farther to the left. In these tissue sections neurons form clusters within the walls of the right and left atria. These clusters continue across many sections, so that when the maps are combined (stacked) across sections, the neurons are thus seen as somewhat continuous columns in the 3D model seen in Figures 2 and 4.

Whereas the qualitative inspection of ICN clustering finds areas of high and low neuronal packing density, a more quantitative and objective approach to these observations involves use the of “partitioning around mediods (PAM)” algorithm to assay packing density or clustering. These clusters can be viewed in TissueMapper in 3D cardiac context (Figure 7A) and without cardiac features as the ICN alone in a posterior point of view (Figure 7B) and, in Figures 7C-E rotated points of view to highlight the shapes of the clusters. These clusters can be represented as surface plots, as in Figure 7F where the height of the surface contour represents the neuronal packing density.

It is possible that, like the neurons in the brain, these clusters and columns of neurons may be somewhat variable in precise spatial distribution but also identifiable as consistently present by coarse-grain anatomical location relative to notable cardiac features. By analyzing the connectivity and molecular phenotype of individual neurons from these clusters it may be possible to identify functional groupings within the ICN. They may have a consistent connectome of functionally specific projections, and may also have distinct molecular phenotypes. The representation of the anatomy of molecular phenotypes of the ICN requires the pipeline described in Figure 1B. Figures 8 & 9 show rat heart sections acquired by this pipeline. Figure 8 presents overviews of regions containing ICN neurons from which LCM samples were acquired, and Figure 9 the detailed neuronal groupings from which single neurons were sampled.

Combining 3D Mapping of the ICN with Laser Capture Microdissection of Single Neurons

The sections in Figures 8&9 are single sections from a female rat heart in which we mapped the 3D organization of the ICN. The heart was sectioned in the transverse plane going rostro-caudally between the base and apex. The tissue sections shown are at regular intervals at levels where ICN neurons are present in the heart. The mapping shows in yellow the position of neurons within the heart at each level. These distributions in two dimensions are like what is seen Figures 2-5 in 3D or stacks, with relatively continuous distributions of neurons that tend to clump in groups consistent with being described as ganglia. Distinct clusters of widely separated cell groups are associated with both atria. Sections are numbered from the base and neurons were found in sections 39 through 470.

The neurons marked with yellow in Figure 9 indicate the single cells mapped to give context of the ICN distribution to support our effort to select cells randomly but broadly representative across the sections. Neurons that were lifted from the tissue by performing laser capture microdissection (LCM) at Z1 levels are marked green (Figure 9 B&C) and those from Z2 levels are marked in blue (Figure 9 D). These 151 single neurons were used to perform single cell transcriptomics. The molecular phenotype of each neuron is associated with the position of each cell in the heart's 3D coordinate framework. The genes expressed and the cell types of these isolated neurons combined back into the specific distributions in 3D context generated by stacking the serial images. This quantitative display can then be used for the visualization of laser capture neurons and linked to their molecular phenotype datasets. Figure 10A&B uses the "data driven" ICN quantitative clustering as was done in Figure 7. However, this ICN was "undersampled" for mapping and is not for comparison to Figure 7. Rather it is to provide context for the clustering and distribution of the neurons lifted for molecular profiling in Figure 10C&D.

Molecular Analysis of Single Neurons in the 3D ICN Context

We obtained a high-throughput transcriptomic data set containing 23,254 data points from 151 samples of both single neurons and neuron pools capturing entire clusters, in total 884 neurons (Figure 11). Each sample was assayed for the expression of 154 genes selected as associated with neuromodulation and cardiac function. We analyzed this transcriptomics data using Principal Component Analysis (PCA) to identify the structured variation, if present, that could organize the neurons into subgroups based on the variability in the gene expression profiles (Figure 12. We mapped the three major neuron groups that arose from PCA results to their spatial location in the three-dimensional coordinates of ICN (Figure 12A). Interestingly, the superior-inferior position

(base to apex direction) accounted for the most robust clustering along PC1 and PC2 (Figure 12). Samples were divided into three Z position groups (Z1, Z2, Z3) where Z1 is closest to the base, moving down to Z3 near the inferior aspect of the atria (Figure 12). Examining the gene expression profiles of samples within the Z groups, distinct sets of genes were distinctly enriched in each of the Z1, Z2, and Z3 positional groups, with a small subset being enriched in both Z2 and Z3 (Figure 12C). Notably, the neurons within each of the Z groups were isolated from multiple ganglia (Figure 11), suggesting that the heterogeneity of molecular phenotypes is more constrained than the spatial distribution of these neurons.

We also analyzed the distribution of select molecular profiles in a pair-wise fashion to assess the alignment of conventionally described cell types in the ICN. For example, a pair-wise comparison of Th and Npy expression demonstrated that while several neurons could be classified as Th only or Npy only, a subset of neurons were Th and Npy positive. These Th+ Npy+ neurons were distributed throughout ICN without any apparent bias towards a narrow spatial location (Figure 12D, left). These results are consistent with results from immunohistochemistry where NPY positive cells and TH positive cells were observed as broadly distributed in the ICN (Richardson et al., 2003), but did not have a correlated expression as was suggested in other results (Crick et al., 1994). Examination of Galanin along with Th, however, shows a more organized pattern with higher expression of Galanin in the Z1 position groups, but with little correlation with Th generally (Figure 12D, right). Interestingly, we found that certain genes showed a very strong spatial localization bias, and examining them in a pairwise manner reveals further co-localization patterns. For example, Cxcr4 and Npff were highly correlated with spatial location. Cxcr4 expression was almost exclusively high in the Z2 and Z3 positional groups, whereas Npff expression was highest in Z3, lowest in Z2, with mid-range of expression in Z1 (Figure 12D, left). Cxr4 and Npff were co-expressed in the neurons in the Z3 positional group. By contrast, the neurons in the Z3 positional group with high expression levels of Npff showed distinctively low expression levels of Dbh, with little correlation between the two genes in Z1 and Z2 neurons (Figure 12D, right). Cxcr4 is also known as the NPY3 receptor, suggesting that these neurons are may be responsive to NPY+ sympathetic fibers infiltrating the heart from the stellate ganglion. Npff has been shown to increase heart rate when acting on receptors in the rat heart, working synergistically with adrenergic signaling pathways (Allard et al., 1995). Using the mapping techniques discussed above, we can also visualize the expression patterns of these genes within the context of their three-dimensional orientation, making it possible for us to delve deeper into the relationship between their expression patterns and locations within the rat ICN (Figure 12).

We evaluated the gene expression for differences in expression between the three Z positional groups using a one-way ANOVA. Hierarchical clustering of samples using the genes with ANOVA $p<0.001$ elucidated four subtypes of neurons (A, B, C, D) (Figure 13), with subtypes A and C being found primarily in the Z1 group, B in the Z2 group, and D in the Z3 group along with a number of samples from the Z1 group (Figure 13A&B). We analyzed the molecular patterns that underlie the spatially organized neuronal subtypes to identify correlated modules of gene expression and the combinations of modules that distinguish each neuronal subtype. For example,we see that comparing Npff to Cxcr4 expression largely delineates the different phenotypes. We saw that Npff and Cxcr4 greatly correlate with spatial position of the Z groupings, where the Z1 group shows a range of expression of Npff. When examining phenotypes, however, we see that phenotype A is largely comprised of cells that have low expression of both Npff and Cxcr4 while phenotype C largely accounts for the cells which show high expression in Npff and low expression of Cxcr4. We also examined the distributions of neuropeptide and corresponding receptor gene expression across the four identified phenotypes. For example, expression patterns between galanin and its receptor, Galr1 show that most cells in phenotype A express high levels of galanin, with a large subset also expressing high levels of Galr1, indicating that cells in phenotype A largely drive galanin signaling both through autocrine signaling as well as the acting as the source for paracrine signaling while cells from phenotypes A, B, and C act as the target for paracrine signaling. Most cells in phenotype D showed low expression for both Gal and Galr1 (Figure 13D&E). Examining expression patterns between thyrotropin release hormone (Trh) and its receptor Trhr show very different connectivity patterns when compared with those for galanin. While a small set of cells from all four phenotypic groups show coexpression of both Trh and Trhr, the most noticeable pattern is that phenotype B has consistently high levels of Trh, but not Trhr, indicating that cells in phenotype B primarily act as the source for paracrine signaling between phenotype B and the other three identified phenotypes.

DISCUSSION

Recapitulation of the major findings and their significance

We find the rat ICN to be a bounded, relatively compact population within the context of the larger 3D anatomy of the heart. It is present on the hilum on the base of the heart on both the left and right side as well as in the interatrial septum. The majority of neurons are on the posterior or dorsal surface of both atria, again on both atria but more prominently on the left side, extending to the coronary sulcus separating the atria from the ventricles. Within the ICN neurons tend to cluster and to some extent appear to form columns in the Z plane or superior-inferior direction. Quantitative analysis of neuronal packing density suggests several distinct groupings, “ganglia”.

The molecular phenotypes of these individual neurons are variable and diverse and reveal many previously unknown neuromodulatory regulators to be present. Spatial analysis shows many of these genes to have specific gradients of expression particularly in the Z plane, and for some of them to specifically associate with the neuronal packing density clusters, suggesting functional specificity by molecular phenotype and location.

These results were made possible by a team science approach involving four groups each providing required technology, as required by the SPARC Program. The approach demonstrated should be applicable to other organs with intrinsic nervous systems. This can be extended to human hearts in health and in heart failure, seeking neuromodulators involved in health and disease. The anatomical and molecular data are all archived in the DAT-CORE of the SPARC Program for public access and use.

The inspiration for our approach comes from the Allen Institute Brain Atlas, which has been at the forefront of brain sectioning and 3D reconstruction (Lein et al., 2007). Micro Bright Field (MBF), which provided relevant technology for the Allen Brain Atlas, are active collaborators in this project. Creating a reference framework and mapping positions of neurons and molecular phenotypes is an ongoing and very active field in brain research, and its extension to the cardiac brain - ICN - benefits from it.

In this paper, we present a method to extract individual neurons in the cardiac ICN and comprehensively record the neurons' relative spatial orientation to the heart at micron resolution. Combined with the ability to extract these neurons for downstream applications, we can now understand the gene expression of individual neurons in the cardiac ICN in their spatial context. Together, we present an integrated pipeline for cardiac connectome and molecular phenotype data acquisition.

Here, we also demonstrate the first use of KESM (knife-edge scanning microscopy) ((McCormick, 2002), US 6,744,572) on cardiac tissue for the purposes of making a cardiac atlas at a micro-level resolution. This process and approach can be expanded to other organ systems for the microscopic mapping of neuronal structures.

State of Anatomical Mapping of Intracardiac Neurons

While qualitative and gross anatomical descriptions of the anatomy of the ICN have been presented, we here bring forth the first comprehensive atlas of the cardiac ICN in rat at a cellular level. This work represents the next logical steps in a long history of attempts to understand the anatomical substrate upon which the neuronal control of cardiac function is built. There has not yet been a comprehensive effort to generate a

neurocardiac atlas for any species, nor any effort to generate a histological mapping at the single neuron level for the whole heart of any species.

However, there have been significant contributions to mapping the nerve bundles in the heart and the locations of ganglia that will be briefly reviewed here. A common technique for several of these studies include immunohistochemical or immunofluorescent staining of a neuronal marker (acetylcholinesterase, tyrosine hydroxylase, choline acetyltransferase, PGP9.5, etc) and examining whole mount with or without microscopy. Mapping efforts of ICN in small animals have included: mouse (Li et al., 2010, 2014; Rysevaite et al., 2011a), rat (Ai et al., 2007; Cheng et al., 2004, 1999; Cheng and Powley, 2000), rabbit (Saburkina et al., 2014), guinea pig (Hardwick et al., 2014; Steele et al., 1994). With these efforts, there was either restricted anatomical regions that were mapped at a microscopic level or large gross anatomical regions that were not mapped microscopically. In most cases, the number of animals used was very low such that the anatomical variability across species is still not well-understood. As has historically been the case across most research domains, these studies often did not include both males and females, so the potential differences in anatomical distributions of ICN between the sexes remains uncharacterized.

The current state of understanding in mapping neurons in the human heart or other large mammals has included examination and quantification of several gross specimens and regional microscopy, but again no comprehensive microscopic atlas has been attempted. In large animal models (describe nature and scope of work done here). In human hearts mapping of fiber tracts and ganglionated plexuses, at a gross anatomical level, have been demonstrated in both whole atrial mounts and gross specimens that were stained and prepared as whole tissue (Pauza et al., 2000; Petraitiene et al., 2014; Singh et al., 1996). While these studies have great merit in determining the potential effects of focal ischemia, ectopic pacemakers, and side effects of tissue ablation, they do not adequately address the molecular substrates that define neuronal behaviors, nor offer a comprehensive microscopic view of the neuronal organizations and projections.

Previous attempts at studying the location of intracardiac ganglia have been done at the gross level, with a limited number of sections at the microscopic level (Armour et al., 1997; Singh et al., 1996). These approaches were not able to comprehensively image the entire heart. Several attempts have shown low-power photomontages of surface tissues following whole-mount staining (Cheng et al., 1999; Richardson et al., 2003). Without tissue clearing technologies, whole mount fluorescent staining is unable to identify regions below 70um of tissue (van Royen et al., 2016). Unlike previous studies, our approach provides an unbiased microanatomy of a continuous region of the heart at the single-cell level.

Other current technologies include tissue clearing reagents followed with various microscopy techniques. Confocal and 2-photon imaging requires laser scanning, which

is slow and hence practical for only small regions. Light sheet microscopy is faster, and has been demonstrated on the murine heart (Ding et al., 2018). This approach also presents an ability to create an unbiased view of the myocardium at the single-cell level. However, there appears to be a trade-off between the physical width of the lightsheet (which can determine the axial resolution) and the size of the volume that can be imaged (Richardson and Lichtman, 2015). Hence lightsheet microscopy with the highest resolution is limited to tissues that are a few hundred micrometers thick. In addition, the electrophoretic process in tissue clearing is not optimal for preservation of charged molecules, including DNA and RNA.

Molecular Heterogeneity of Cardiac Neurons

The current understanding of ICN is that they are capable at least of modulating cardiac physiological functions of chronotropy, dromotropy, inotropy, and lusitropy . Several anatomical studies have revealed the complexity of cardiac ganglia organization both in the cell body locations (Hasan, 2013; Hoover et al., 2009; Li et al., 2014; Pauziene et al., 2016; Rysevaite et al., 2011b, 2011a; Saburkina et al., 2014) and the complexity of afferent and efferent projections to and from the ICN (Cheng et al., 2004, 1999; Cheng and Powley, 2000; Lin et al., 2014; Li et al., 2014, 2010). While some work has hinted at the vast heterogeneity of the ICN from a functional (Beaumont et al., 2013) perspective, there has not yet been a systematic assay interrogating the molecular substrates that underlies this functional heterogeneity. From a population perspective, it is exactly this type of heterogeneity that may determine the differences between patients who respond to vagal stimulation and those who do not. Furthermore, determination of the deficits in the ICN that drive cardiovascular pathology can lead to new avenues of therapy not only for patients with heart failure, but also with a preventative approach as the transition from health to disease is better understood from the perspective of the ICN (Herring, 2015; Li et al., 2014; Longpré et al., 2014). This work represents the first that we are aware of that attempts to elucidate the transcriptional heterogeneity of anatomically positioned ICN in the rat heart., providing anatomical and molecular substrates for functional heterogeneity of cardiac ICNs.

The distinct molecular phenotypes that are defined along the Z axis (base-to-apex axis) have not been previously described. That such an organizational pattern exists may be a result of the embryological development of the intrinsic cardiac ganglia, predominantly from the migration of neural crest cells that differentiate into neurons. The migrating neural crest cells enter the heart at the base, spread out within the atria toward the apex (Fukiishi and Morriss-Kay, 1992; Hildreth et al., 2008). As in the brain, neurons in the heart likely follow chemical gradients to determine the direction and extent of migration, offering a possible explanation for why molecular phenotypes can be defined along the Z axis and opening the door for further work to determine which molecules make up

these gradients. That cardiac conduction runs generally from base to apex may also suggest a functional implication for the separation of neurons in this fashion. In mouse hearts, not all intracardiac ganglia originate from migrating neural crest cells, especially those that influence nodal pacemakers (Hildreth et al., 2008). Further development of more comprehensive profiling of single neurons within their anatomical context will provide important information as to the role of both neural crest and non neural crest neurons in the heart.

Data Framework

In order to piece together the relationship between 3D histological reconstructions and single cell molecular data, data storage and annotation must be carefully considered. Not only does the use of an anatomical ontology provide a means by which neurons can be anatomically referred to, but also makes it so that data from different hearts can be more readily compared. The generation of such data storage and annotation is not a trivial matter and requires collaboration between technicians, researchers, software developers, and data storage specialists. While purely mathematical and statistical methods for interpreting these data are crucial, the complexity quickly gets to a point where such approaches are challenging, making the ability to qualitatively interpret the data essential. To this end, MBF has designed custom software, TissueMaker and TissueMapper, allowing for visualization of molecular and anatomical patterns. All processed and raw data are available in the NIH SPARC data repositories designed and curated by Blackfynn.

Future directions for scalability and extension

We have established approaches that will now support scaling to acquire more precisely several male and female ICN providing a 3D framework as a foundational data resource - useful to developing detailed anatomical neural circuit/connectomic maps for neural control of the heart, and showing 3D distribution/gradients of molecular phenotypes. This unprecedented granularity in the understanding of cardiac neurons has the potential to unlock a new generation of cardiac therapeutics to treat or prevent all manner of cardiac pathology.

To achieve the desired integration of different datatypes, the data from other approaches are visualized within the ICN of the KESM 3D framework.
The demonstration of cross-species application of the approach supports scaling to organisms with larger and more complex hearts such and pig and man, and to extension to other organs.

METHODS

Figure 1 illustrates our two approaches as two graphical workflows. We established two multi-component pipelines to map neurons mapped from histological heart tissue sections. One approach optimizes precision of 3D heart shape and tissue section alignment for establishing a 3D reference framework. The second trades resolution of cardiac structure for, in addition to mapping neuron positions, the acquisition of projections/connectomic data and/or acquisition of neuron samples for molecular profiling. **Figure 1A shows the first pipeline** that acquires sections and images by using the novel Knife Edge Scanning Microscopy system (KESM, 3Scan) which maintains precision and eliminates most artifacts. **Figure 1B shows the second pipeline**, using cryostat sectioning, used here for a male and female rat heart. Images of these sections, including cell positions, can be stacked to create a whole heart volume with data that can be brought into the 3D reference systems created by the first approach.

Schematic representation of KESM equipment setup

Heart samples that are fixed and Nissl-stained are embedded into a paraffin or resin mold prior to mounting onto an XYZ robotic stage. The robotic stage will move the sample along the diamond knife ultramicrotome that is coupled to a fiber optic. The sample is illuminated by the fiber optic as it is cut with the diamond knife and simultaneously scanned line-by-line and imaged at 10X objective to produce an image file of a single section.

Images taken by KESM have the great advantages for precision of gross morphology while resting on cell-level histology, ideal for developing 3D frameworks to hold additional data types from other approaches. Using the TissueMapper software (MBF Biosciences) to map the position of each neuron as illustrated in Figure 2 we develop a comprehensive mapping of the precise extent and distribution of the ICN in the 3D framework of the heart.

Rat heart processing for constructing a 3D framework

A normal male rat heart was obtained fresh and subsequently immersed in 4% paraformaldehyde prior to whole-mount diffusion staining with Cresyl Echt Violet stain (0.05g in 50ml dH_2O + 150µl glacial acetic acid, for 7 days) to enable visualization of the intrinsic cardiac neurons and ganglia. 5µm sections were cut and section images were simultaneously acquired by Knife Edge Scanning Microscopy (KESM, 3Scan, San Francisco), a proprietary serial section microscopy platform for 3D volumetric imaging. KESM uses a diamond knife ultramicrotome, coupled to a nano-positioned robotic stage, and proprietary optics to produce 3D images of large tissue blocks at micron-scale resolution. The 5mm blade moves across the surface of a block of tissue, slicing and scanning simultaneously, capturing one line of image data at a time (at 10 X

magnification) via high-speed line-scan camera, to generate an image tile comprised of 10,000 pixels, with each pixel representing 0.5μm. Post-processing of the data utilizes the precise spatial alignment provided by the KESM technique to generate 2D image planes, which were subjected to denoising and artefact reduction. Individual image planes were assembled together into a 3D volume, enabling quantification of morphological details over large anatomical distances. To achieve this, individual KESM image tiles acquired from each XY location at each Z position were automatically aligned and stitched into 2D image planes, and then assembled into a 3D image volume using custom software (MBF Bioscience, Williston). These image volumes were annotated using TissueMapper as described below.

Software Development and Neuron Mapping

A custom suite of computational mapping programs has been developed for mapping neurons (or any cell of interest) in organs including the heart: TissueMaker and TissueMapper. These were, and continue to be, evolved from the tools MBF Biosciences has developed for brain mapping, such as Neurolucida.

The rat heart sectioned at TJU was run through the Tissue Maker and TissueMapper pipeline. By contrast, the KESM image data from 3Scan skipped the TissueMaker step because it was already spatially aligned.

Using TissueMaker software, the section images were then extracted from the whole slide image, cropped to a uniform size, the perimeter automatically segmented, and aligned spatially by identifying the centroid of each section to generate an image stack. The heart image volume was then shared with TJU and UCF for further mapping and segmentation using custom-developed software (TissueMapper; MBF Bioscience). The software application includes annotation tools for automatically or manually drawing regions, placing markers to indicate cell positions and other discrete points, and the ability to import comprehensive lists of regions as a text or comma-delimited file.

As is illustrated in this movie (https://mbfbioscience.sharefile.com/d-sa1501de2ad94d3f9) precise locations of each cardiac neuron were mapped in all sections in which neurons are present. In addition to marking the cell location, numerous regions selected from the comprehensive ontology first generated for the Cardiac Physiome Project (Hunter and Smith, 2016) were mapped. Of the thousands of ontological features that were available, less than 40 were selected for these initial representations in order to simplify the images and to test the pipeline more efficiently. On each section, researchers traced key features (aorta, pulmonary vessels, atrial borders, etc.) and to identified neurons based upon a combination of Nissl staining and morphology. The TissueMaker and TissueMapper software are then able to generate

3D wireframes of the hearts with neurons positioned in context. Attributes like color and shape can be customized in these reconstructions and quantitative spatial data can be obtained. By mapping anatomical fiducial information alongside the neuron locations, the extent and location of the neurons within the larger context of the entire heart could be viewed as a 3D representation, as seen in the Figures for the present work.

Cryosectioning and Embedding

In our initial efforts with Heart A (male) and Heart B (female) we learned that, unlike the brain, the distortions of the heart are far less homogenous and symmetric, which can interfere with data visualization and comparison between specimens. Thus we developed the method described below and presented in this movie (https://mbfbioscience.sharefile.com/d-sa1501de2ad94d3f9) to keep the chambers inflated. We also discovered that the embedding media needs color added to permit image segmentation. Optimal Cutting Temperature media (OCT, TissueTek) is added to an embedding mold, to cover the bottom of the mold and kept on dry ice. Three concentrations of OCT diluted in 1x PBS are prepared 25% 50%, and 100%. The 100% OCT preparation should include a few drops of green food grade dye to permit optimal image segmentation of any subsequent blockface images. The animal is sacrificed using rapid decapitation after 60 seconds of exposure to 5% isoflurane. The heart is immediately excised and submerged in room temperature 1x PBS for 30 seconds or until the majority of blood is pumped out of the chambers. The still beating heart is transferred to 25% OCT, and lightly agitated for 30-60 seconds. This is then transferred to a 50% OCT solution, and lightly agitated for 30-45 seconds. Ideally, the heart should still be beating at this point. The large chambers of the heart should be injected with colored OCT using a 14-16 gauge blunt needle on a syringe in order to mitigate structural collapse during cryosectioning. Next, the heart is placed in a chilled embedding mold. Room-temperature OCT is added to completely submerge the heart. The mold is then placed in a slurry of dry ice and methanol to promote rapid freezing. Care should be taken to avoid allowing methanol to come into contact with the OCT inthe block as this will compromise the structural integrity of the OCT once frozen. Holding the block near liquid nitrogen, but not submerging it, is also a means of rapid cooling. After the OCT is completely frozen, it is covered with aluminum foil and then in a plastic wrap to prevent accumulation of condensation in the mold. The mold is transferred to a -80°C freezer. Ideally the entire process should happen within 5-10 minutes to mitigate RNA degradation, which will be necessary for future investigations of single cell transcriptomics using laser capture microdissection.

Slide Preparation

Heart A was sectioned from base to apex at 20um, yielding nearly 800 sections, with corresponding blockface images, and mounted onto 400 slides (two sections per slide).

In order to appreciate a finer level of detail and clarify tissue staining, Heart B was sectioned at 10 um yielding nearly 1600 sections mounted on 800 slides with block face images for each section.

Each slide was stained with 0.1% cresyl violet and dehydrated using increasing concentrations of ethanol and xylene. Cover slips were added using mounting media and slides were then imaged using a slide scanner equipped with 20x Olympus objective (N.A.= 0.75; Bliss-200, MBF Bioscience, Williston, VT). On average, 2,000 image tiles were automatically acquired and stitched to create a high-resolution whole slide image containing two heart sections per image.

Laser capture microdissection

In order to isolate neurons while maintaining their anatomical origin in three dimensional space, it was necessary to use laser capture microdissection (Arcturus, ThermoFisher). Neurons were visualized using a rapid cresyl violet stain that highlighted the histological appearance of neurons and maintained RNA quality. Single neurons and pools of single neurons were collected on Capsure HS caps and the cells lysed right on the cap within 15 minutes after laser capture using lysis buffer from the CellsDirect DNA extraction kit (Life Technologies).

Transcriptomics of ICN enriched cardiac tissue

All procedures involving the use of live animals were approved by the Thomas Jefferson University Institutional Animal Care and Use Committee (IACUC). Adult male and female Sprague Dawley rats, 15-16 weeks old, were briefly anesthetized using 5% isoflurane before sacrifice by rapid decapitation. The heart was excised and rinsed briefly in normal saline before dissection under a surgical microscope to remove the excess distal aspects of the great vessels and connective tissue while maintaining the fat pads. The superior half of the atria closest to the base was removed as the neuronally enriched sample. The tip of the auricles and superior aspect of the ventricles comprised the myocardium enriched sample. Each tissue sample was immediately freeze clamped in liquid nitrogen to preserve the RNA and to aid pulverization prior to extraction. RNA extraction was performed using the RNeasy Mini-Prep (Qiagen) according to manufacturer recommended protocols. Microarrays were used to perform transcriptomic assays on all samples by the Thomas Jefferson University Cancer Genomics Core using the Clariom S Assay for rat from Affymetrix.

Transcriptional assay of laser captured single neurons and pools using multiplex RT-qPCR

In order to assay single neurons and neuron pools from laser capture, it was necessary to apply multiplex RT-qPCR to ensure the sensitivity to detect several genes of interest given the small amount of RNA per sample. The Biomark HD microfluidic system (Fluidigm) was used for all gene expression assays. After reverse transcription and whole transcriptome amplification (WTA kit Qiagen) the samples were processed through the Biomark system following manufacturer suggested protocols. Quality control of RT-qPCR results included filtering through melt-curve analysis along with automatic C_t thresholding to determine the limit of detection (Fluidigm).

Bibliography

Ai, J., Gozal, D., Li, L., Wead, W.B., Chapleau, M.W., Wurster, R., Yang, B., Li, H., Liu, R., Cheng, Z., 2007. Degeneration of vagal efferent axons and terminals in cardiac ganglia of aged rats. J. Comp. Neurol. 504, 74–88. doi:10.1002/cne.21431

Allard M, Labrouche S, Nosjean A, Laguzzi R. Mechanisms underlying the cardiovascular responses to peripheral administration of NPFF in the rat. J Pharmacol Exp Ther. 1995 Jul;274(1):577-83. PubMed PMID: 7616447.

Armour, J.A., Murphy, D.A., Yuan, B.X., Macdonald, S., Hopkins, D.A., 1997. Gross and microscopic anatomy of the human intrinsic cardiac nervous system. Anat. Rec. 247, 289–298. doi:10.1002/(SICI)1097-0185(199702)247:2<289::AID-AR15>3.0.CO;2-L

Beaumont, E., Salavatian, S., Southerland, E.M., Vinet, A., Jacquemet, V., Armour, J.A., Ardell, J.L., 2013. Network interactions within the canine intrinsic cardiac nervous system: implications for reflex control of regional cardiac function. J Physiol (Lond) 591, 4515–4533. doi:10.1113/jphysiol.2013.259382

Cheng, Z., Powley, T.L., 2000. Nucleus ambiguus projections to cardiac ganglia of rat atria: an anterograde tracing study. J. Comp. Neurol. 424, 588–606. doi:10.1002/1096-9861(20000904)424:4<588::AID-CNE3>3.0.CO;2-7

Cheng, Z., Powley, T.L., Schwaber, J.S., Doyle, F.J., 1999. Projections of the dorsal motor nucleus of the vagus to cardiac ganglia of rat atria: an anterograde tracing study. J. Comp. Neurol. 410, 320–341. doi:10.1002/(SICI)1096-9861(19990726)410:2<320::AID-CNE12>3.0.CO;2-5

Cheng, Z., Zhang, H., Guo, S.Z., Wurster, R., Gozal, D., 2004. Differential control over postganglionic neurons in rat cardiac ganglia by NA and DmnX neurons: anatomical evidence. Am. J. Physiol. Regul. Integr. Comp. Physiol. 286, R625-33. doi:10.1152/ajpregu.00143.2003

Crick, S.J., Wharton, J., Sheppard, M.N., Royston, D., Yacoub, M.H., Anderson, R.H., Polak, J.M., 1994. Innervation of the human cardiac conduction system. A quantitative immunohistochemical and histochemical study. Circulation 89, 1697–1708.

Ding, Y., Bailey, Z., Messerschmidt, V., Nie, J., Bryant, R., Rugonyi, S., Fei, P., Lee, J., Hsiai, T.K., 2018. Light-sheet Fluorescence Microscopy for the Study of the Murine Heart. J. Vis. Exp. doi:10.3791/57769

Fukiishi, Y., Morriss-Kay, G.M., 1992. Migration of cranial neural crest cells to the pharyngeal arches and heart in rat embryos. Cell Tissue Res. 268, 1–8. doi:10.1007/BF00338048

Hardwick, J.C., Ryan, S.E., Beaumont, E., Ardell, J.L., Southerland, E.M., 2014. Dynamic remodeling of the guinea pig intrinsic cardiac plexus induced by chronic myocardial infarction. Auton. Neurosci. 181, 4–12. doi:10.1016/j.autneu.2013.10.008

Hasan, W., 2013. Autonomic cardiac innervation: development and adult plasticity. Organogenesis 9, 176–193. doi:10.4161/org.24892

Herring, N., 2015. Autonomic control of the heart: going beyond the classical neurotransmitters. Exp. Physiol. 100, 354–358. doi:10.1113/expphysiol.2014.080184

Hildreth, V., Webb, S., Bradshaw, L., Brown, N.A., Anderson, R.H., Henderson, D.J., 2008. Cells migrating from the neural crest contribute to the innervation of the venous pole of the heart. J. Anat. 212, 1–11. doi:10.1111/j.1469-7580.2007.00833.x

Hoover, D.B., Isaacs, E.R., Jacques, F., Hoard, J.L., Pagé, P., Armour, J.A., 2009. Localization of multiple neurotransmitters in surgically derived specimens of human atrial ganglia. Neuroscience 164, 1170–1179. doi:10.1016/j.neuroscience.2009.09.001

Hunter, P.J., Smith, N.P., 2016. The cardiac physiome project. J Physiol (Lond) 594, 6815–6816. doi:10.1113/JP273415

Lein, E.S., Hawrylycz, M.J., Ao, N., Ayres, M., Bensinger, A., Bernard, A., Boe, A.F., Boguski, M.S., Brockway, K.S., Byrnes, E.J., Chen, Lin, Chen, Li, Chen, T.-M., Chin, M.C., Chong, J., Crook, B.E., Czaplinska, A., Dang, C.N., Datta, S., Dee, N.R., Jones, A.R., 2007. Genome-wide atlas of gene expression in the adult mouse brain. Nature 445, 168–176. doi:10.1038/nature05453

Lin, M., Hatcher, J.T., Wurster, R.D., Chen, Q.-H., Cheng, Z.J., 2014. Characteristics of single large-conductance Ca2+-activated K+ channels and their regulation of action potentials and excitability in parasympathetic cardiac motoneurons in the nucleus ambiguus. Am J Physiol, Cell Physiol 306, C152-66. doi:10.1152/ajpcell.00423.2012

Li, L., Hatcher, J.T., Hoover, D.B., Gu, H., Wurster, R.D., Cheng, Z.J., 2014. Distribution and morphology of calcitonin gene-related peptide and substance P immunoreactive axons in the whole-mount atria of mice. Auton. Neurosci. 181, 37–48. doi:10.1016/j.autneu.2013.12.010

Li, L., Huang, C., Ai, J., Yan, B., Gu, H., Ma, Z., Li, A.Y., Xinyan, S., Harden, S.W., Hatcher, J.T., Wurster, R.D., Cheng, Z.J., 2010. Structural remodeling of vagal afferent innervation of aortic arch and nucleus ambiguus (NA) projections to cardiac ganglia in a transgenic mouse model of type 1 diabetes (OVE26). J. Comp. Neurol. 518, 2771–2793. doi:10.1002/cne.22363

Longpré, J.-P., Salavatian, S., Beaumont, E., Armour, J.A., Ardell, J.L., Jacquemet, V., 2014. Measure of synchrony in the activity of intrinsic cardiac neurons. Physiol. Meas. 35, 549–566. doi:10.1088/0967-3334/35/4/549

McCormick, D.A., 2002. Cortical and subcortical generators of normal and abnormal rhythmicity. Int. Rev. Neurobiol. 49, 99–114.

Pauza, D.H., Skripka, V., Pauziene, N., Stropus, R., 2000. Morphology, distribution, and

variability of the epicardiac neural ganglionated subplexuses in the human heart. The Anatomical Record.

Pauziene, N., Alaburda, P., Rysevaite-Kyguoliene, K., Pauza, A.G., Inokaitis, H., Masaityte, A., Rudokaite, G., Saburkina, I., Plisiene, J., Pauza, D.H., 2016. Innervation of the rabbit cardiac ventricles. J. Anat. 228, 26–46. doi:10.1111/joa.12400

Petraitiene, V., Pauza, D.H., Benetis, R., 2014. Distribution of adrenergic and cholinergic nerve fibres within intrinsic nerves at the level of the human heart hilum. Eur J Cardiothorac Surg 45, 1097–1105. doi:10.1093/ejcts/ezt575

Richardson, D.S., Lichtman, J.W., 2015. Clarifying Tissue Clearing. Cell 162, 246–257. doi:10.1016/j.cell.2015.06.067

Richardson, R.J., Grkovic, I., Anderson, C.R., 2003. Immunohistochemical analysis of intracardiac ganglia of the rat heart. Cell Tissue Res. 314, 337–350. doi:10.1007/s00441-003-0805-2

Rysevaite, K., Saburkina, I., Pauziene, N., Noujaim, S.F., Jalife, J., Pauza, D.H., 2011a. Morphologic pattern of the intrinsic ganglionated nerve plexus in mouse heart. Heart Rhythm 8, 448–454. doi:10.1016/j.hrthm.2010.11.019

Rysevaite, K., Saburkina, I., Pauziene, N., Vaitkevicius, R., Noujaim, S.F., Jalife, J., Pauza, D.H., 2011b. Immunohistochemical characterization of the intrinsic cardiac neural plexus in whole-mount mouse heart preparations. Heart Rhythm 8, 731–738. doi:10.1016/j.hrthm.2011.01.013

Saburkina, I., Gukauskiene, L., Rysevaite, K., Brack, K.E., Pauza, A.G., Pauziene, N., Pauza, D.H., 2014. Morphological pattern of intrinsic nerve plexus distributed on the rabbit heart and interatrial septum. J. Anat. 224, 583–593. doi:10.1111/joa.12166

Singh, S., Johnson, P.I., Lee, R.E., Orfei, E., Lonchyna, V.A., Sullivan, H.J., Montoya, A., Tran, H., Wehrmacher, W.H., Wurster, R.D., 1996. Topography of cardiac ganglia in the adult human heart. J. Thorac. Cardiovasc. Surg. 112, 943–953. doi:10.1016/S0022-5223(96)70094-6

Steele, P.A., Gibbins, I.L., Morris, J.L., Mayer, B., 1994. Multiple populations of neuropeptide-containing intrinsic neurons in the guinea-pig heart. Neuroscience 62, 241–250. doi:10.1016/0306-4522(94)90327-1

van Royen, M.E., Verhoef, E.I., Kweldam, C.F., van Cappellen, W.A., Kremers, G.-J., Houtsmuller, A.B., van Leenders, G.J.L.H., 2016. Three-dimensional microscopic analysis of clinical prostate specimens. Histopathology 69, 985–992. doi:10.1111/his.13022

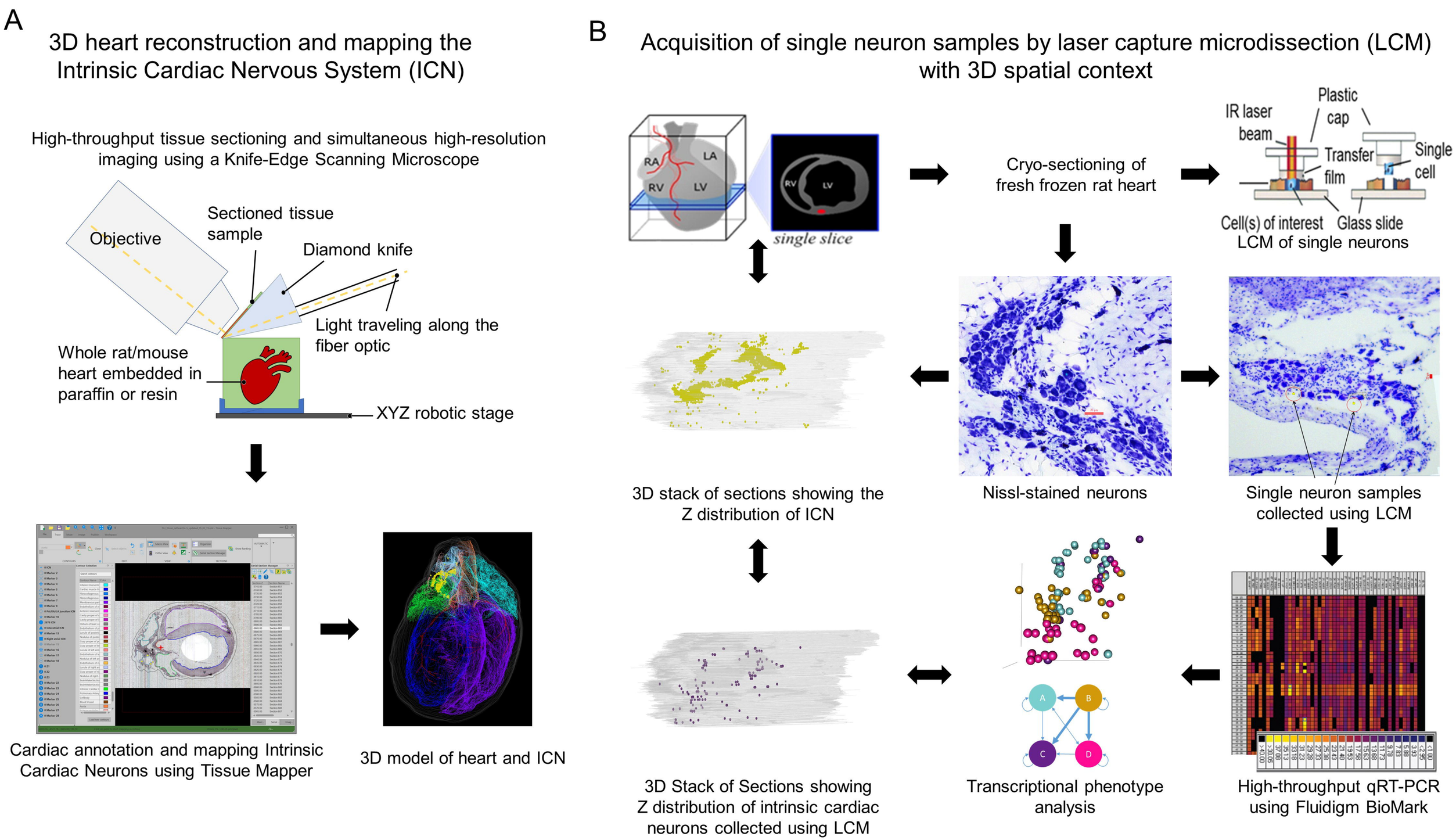

Figure 1. Data Acquisition Pipelines (**A**) Acquisition of a 3D, accurate organ reference framework using high resolution collection of histological tissue sections. Once the entire heart is sectioned and imaged, the images are then compiled into an image volume by the TissueMaker software to enable 3D heart reconstruction and ICN mapping with the TissueMapper software. (**B**) Acquisition of cresyl violet stained neuronal samples from fresh heart tissue by cryostat sectioning. Single neurons were identified by position in the ICN and lifted for qPCR or RNA-Seq molecular phenotyping.

Posterior view of intrinsic cardiac neurons

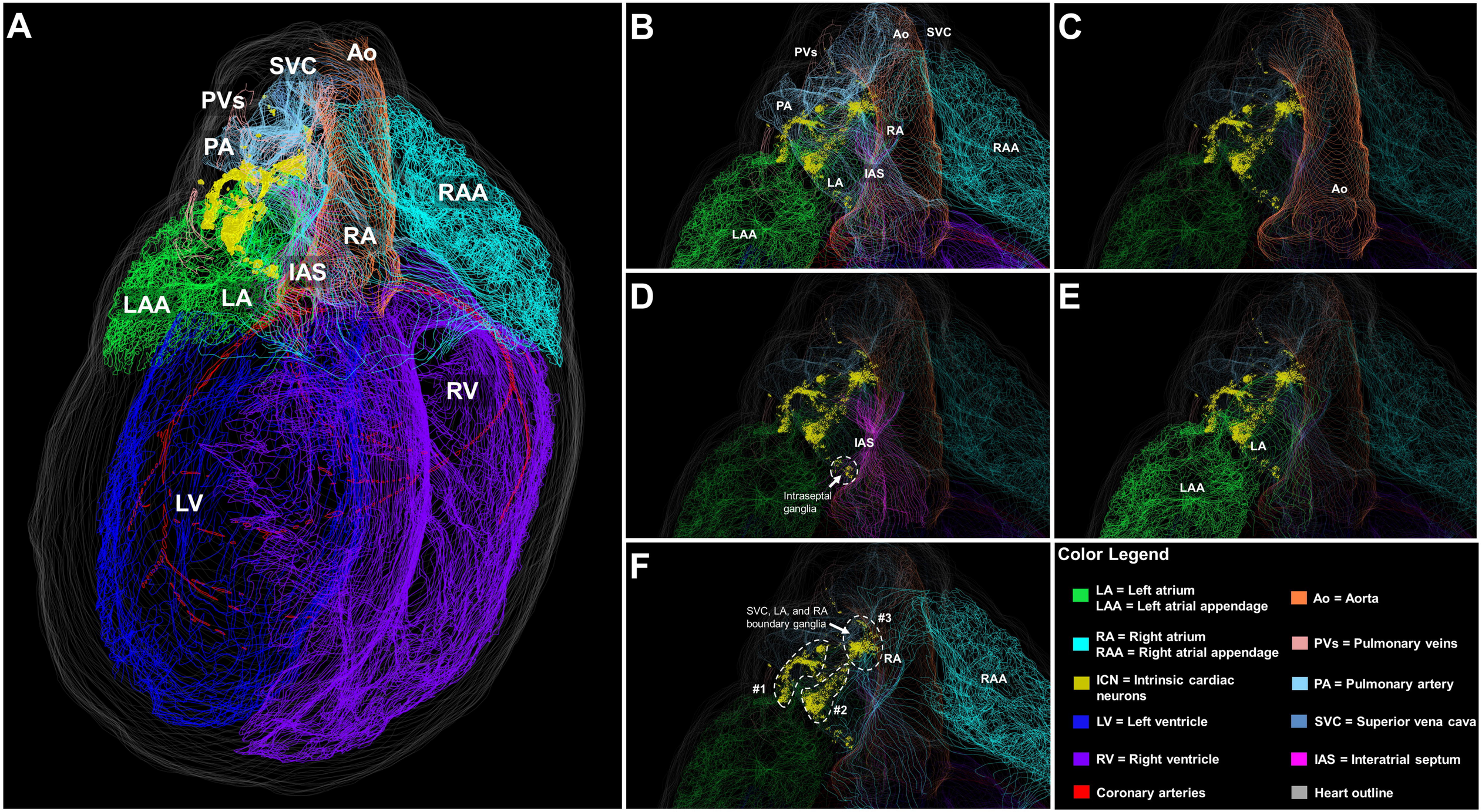

Figure 2. Posterior view of the 3D reconstructed male rat heart. (A) Whole-heart view showing the context, extent and distribution of the intrinsic cardiac neurons (ICN), located on superior and posterior surfaces of the atria. (**B-F)** take a higher-resolution view outlined by the rectangle in **(A)**, which is shown in **(B)**, with various contoured features of heart anatomy are selectively removed to appreciate the anatomical relationship of the ICN to **(C)** the aorta, **(D)** the interatrial septum, **(E)** the left atrium and **(F)** the right atrium, where clusters #1 and #2 appear to be on the surface of both atria, while cluster #3, located around the border of the superior vena cava, left atrium, and right atrium appears on the right atrium.

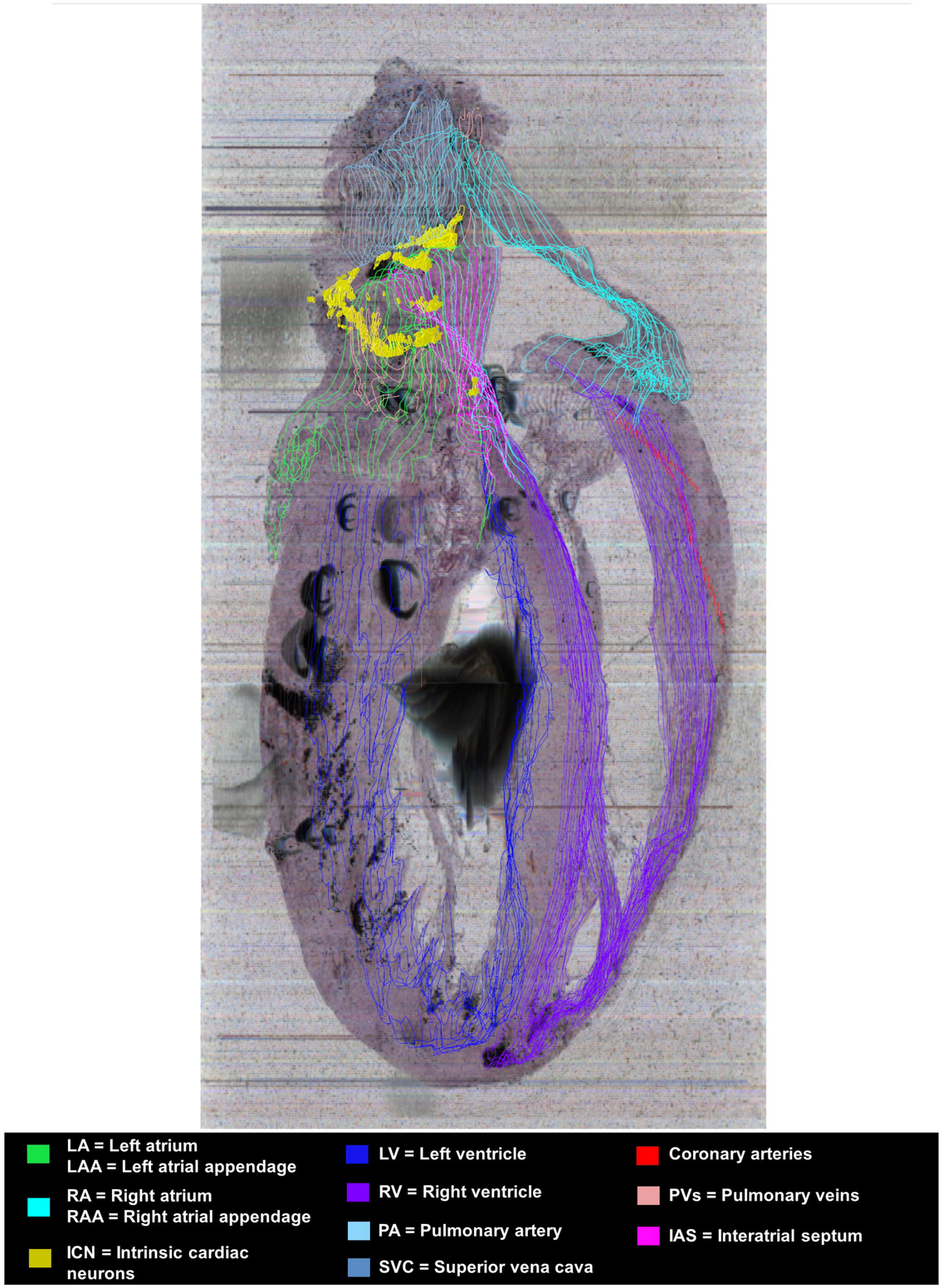

Figure 3. ICN distribution in a partial projection of sagittal heart sections. A partial projection of contours and ICN in a 3mm thick sagittal image slab illustrate the distribution of neurons along the superior-inferior extent of the heart.

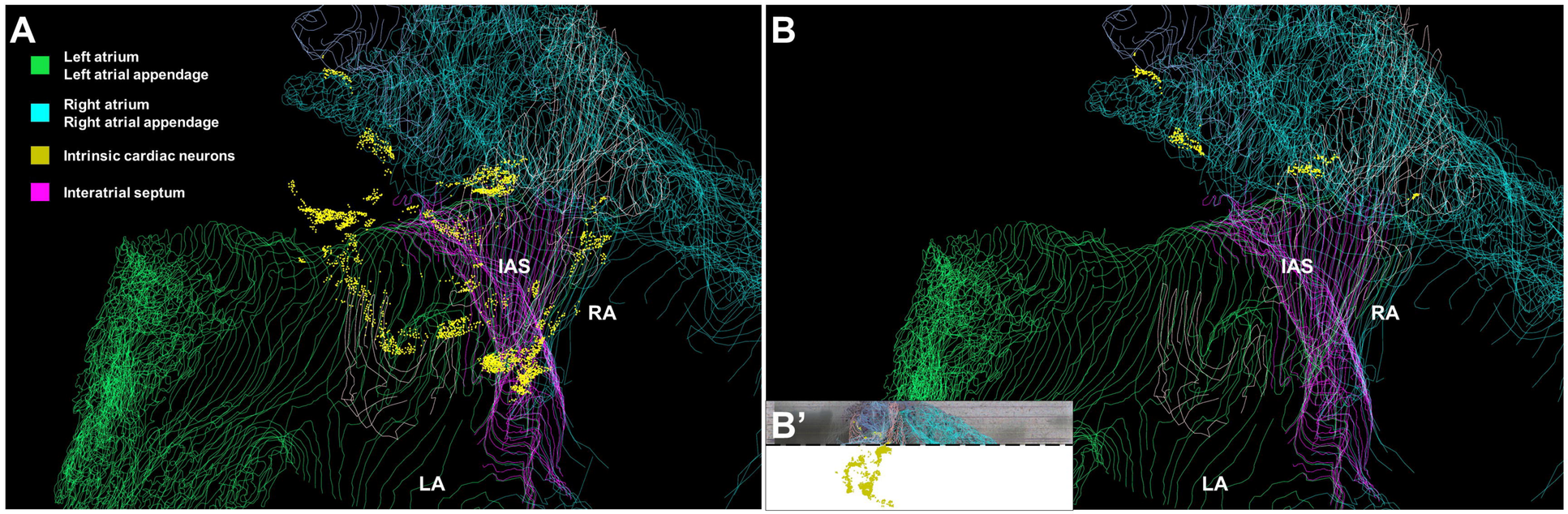

Figure 4. Superior view of the ICN. (A) Viewing the ICN distribution (neurons mapped as yellow dots) looking from the base towards the apex. The left and right distribution of all ICN neurons is discriminated by their relationship to the interatrial septum. Note that most ICN neurons visualized in **(A)** are not all on the base of the heart but mostly distributed at more inferior-caudal levels of the heart on both atria. **(B')** In order to selectively view those neurons on the base of the heart we took this posterior view of the full ICN and retained only those above the cut-off point indicated by the dotted black line. **(B)** Then these neurons are here observed from the superior view of the heart, showing the position of ICN neurons located within the hilum in between the aorta, superior vena cava, pulmonary artery.

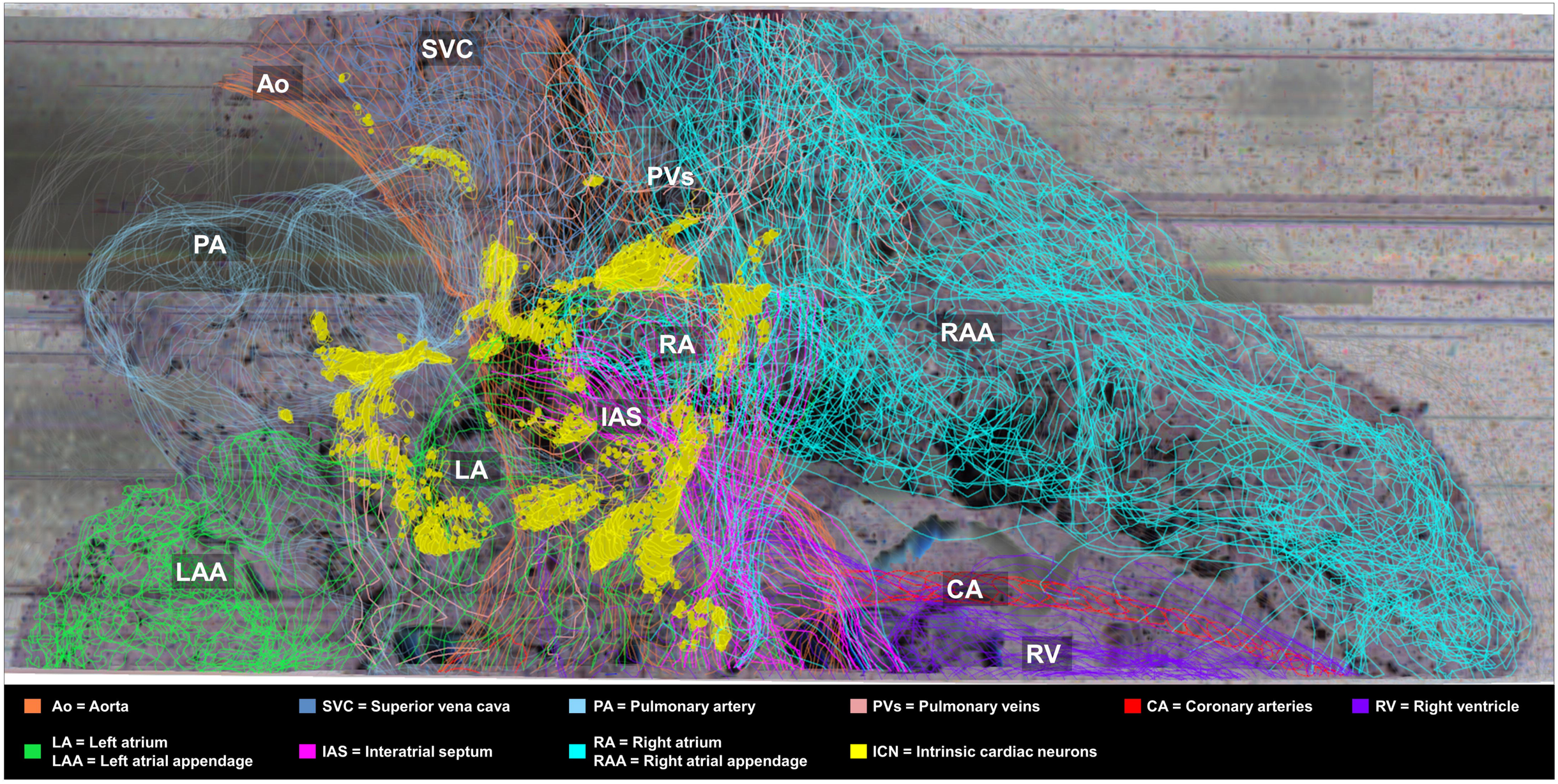

Figure 5. Distribution of more inferiorly located ICN. Using the TissueMapper Partial Projection tool that visualizes the ICN in a 3mm thick transverse image slab rotated in a superior view. This illustrates the locations in the transverse plane of section to highlight more inferiorly (caudally) located neurons. Neurons are represented as yellow dots.

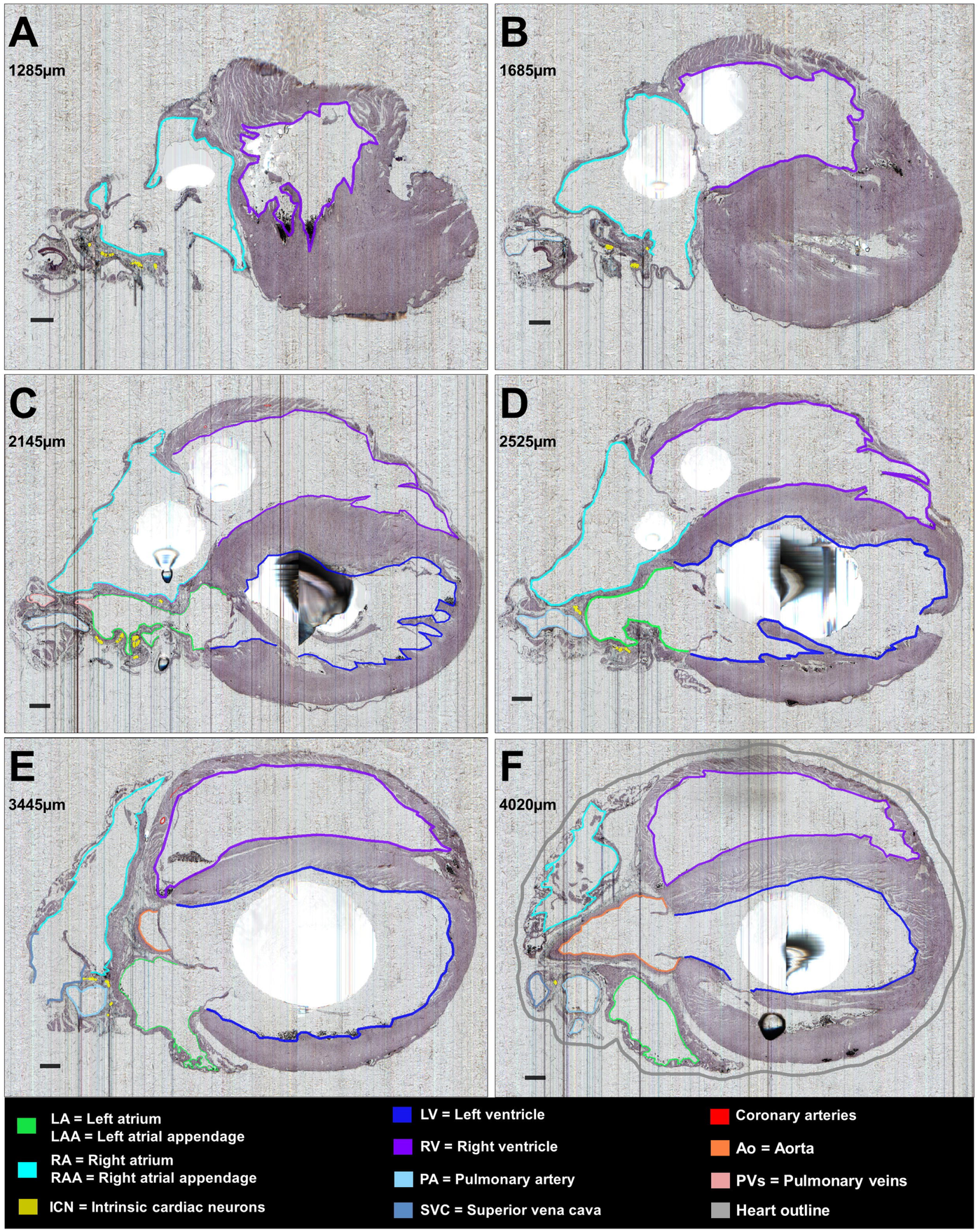

Figure 6. ICN distribution at six different semi-sagittal

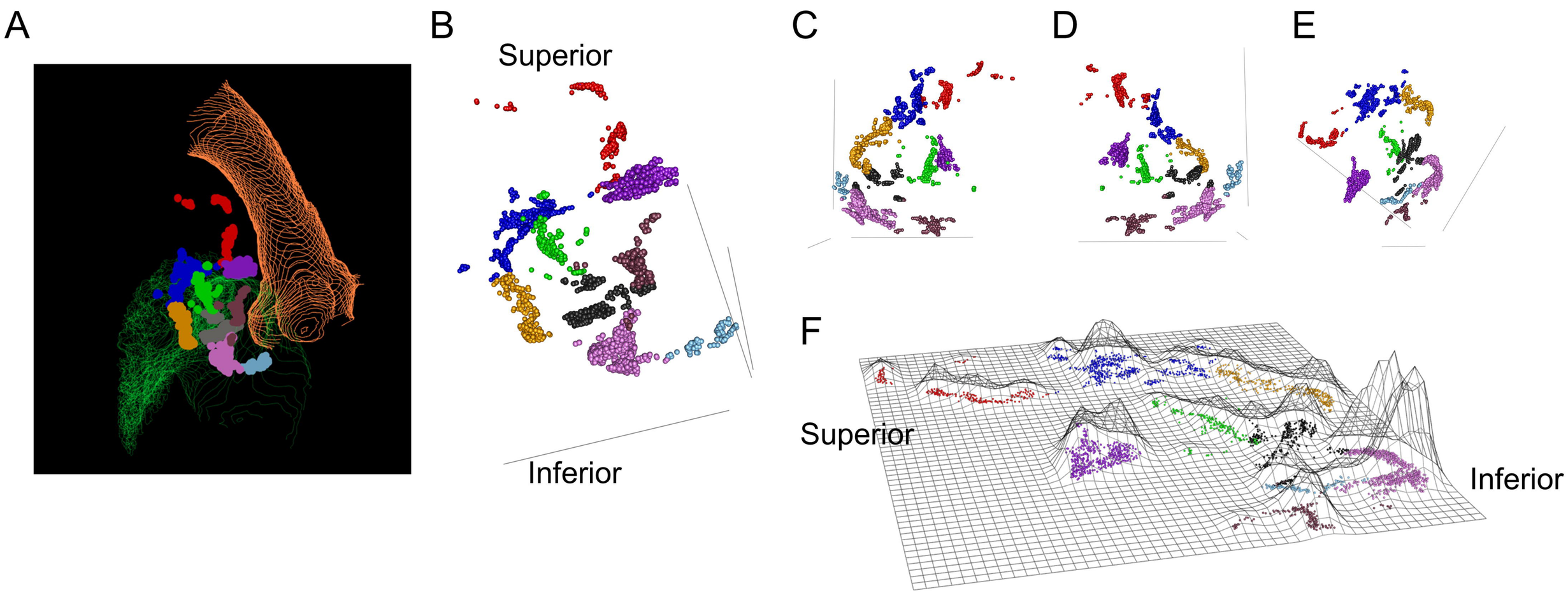

Figure 7. Identification of Neuronal Clusters in the Rat heart. Nine clusters of neurons were identified using the partitioning around medoids (PAM) algorithm, where identified clusters are shown in different colors. **(A)** Visualization of mapped neurons in their 3D orientation in TissueMapper, contours show the Aorta (orange) as well as the Left Atrium (green). **(B)** Visualization of mapped neurons in their 3D orientation. **(C-E)** Visualization of mapped neurons in their 3D orientation rotated to show different points of view. **(F)** Flat-mount projection of mapped neurons where the height of the contours are proportional the density of neurons. The orientation in (E) matches the flat-mount projection in (F).

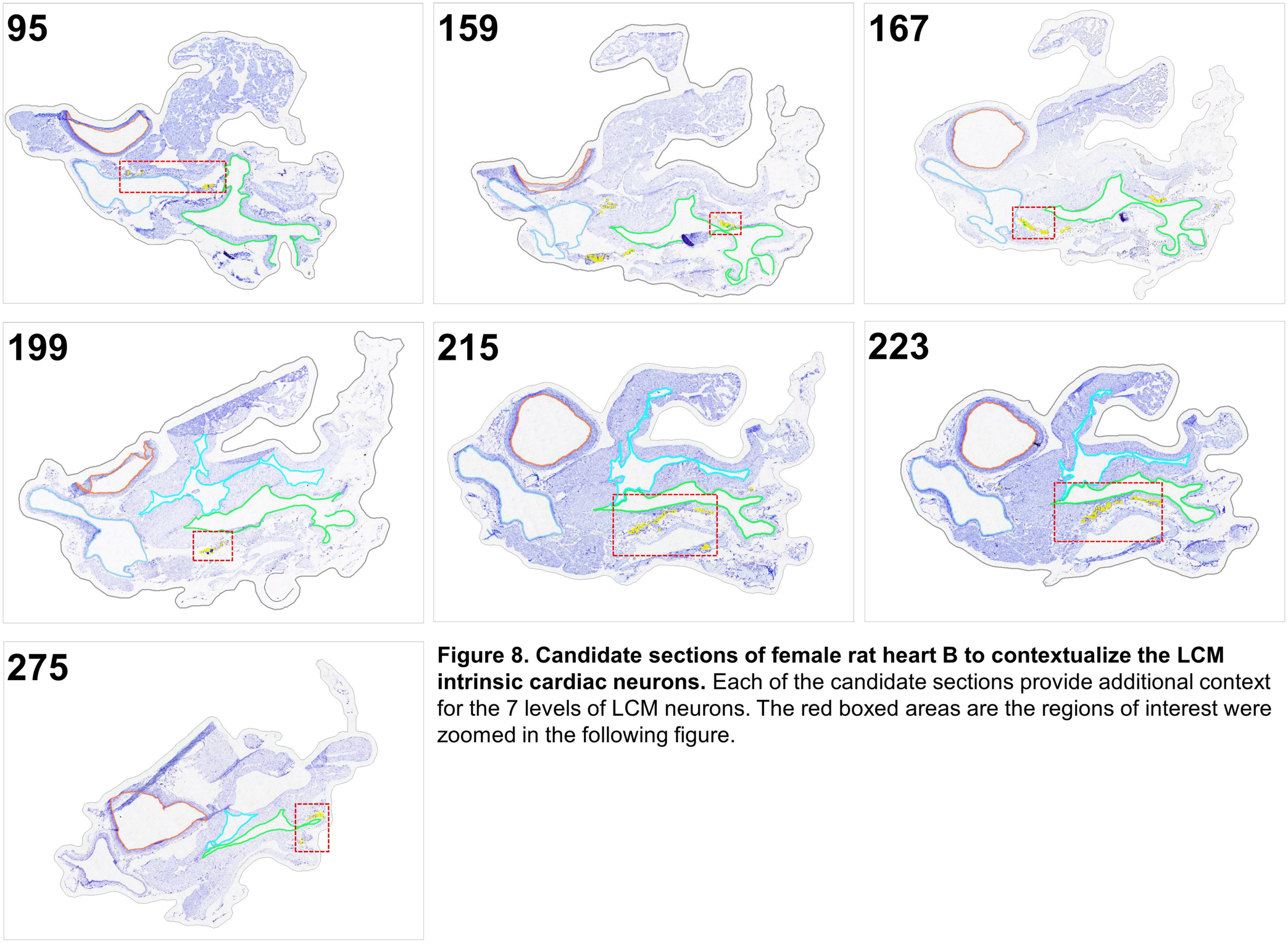

Figure 8. Candidate sections of female rat heart B to contextualize the LCM intrinsic cardiac neurons. Each of the candidate sections provide additional context for the 7 levels of LCM neurons. The red boxed areas are the regions of interest were zoomed in the following figure.

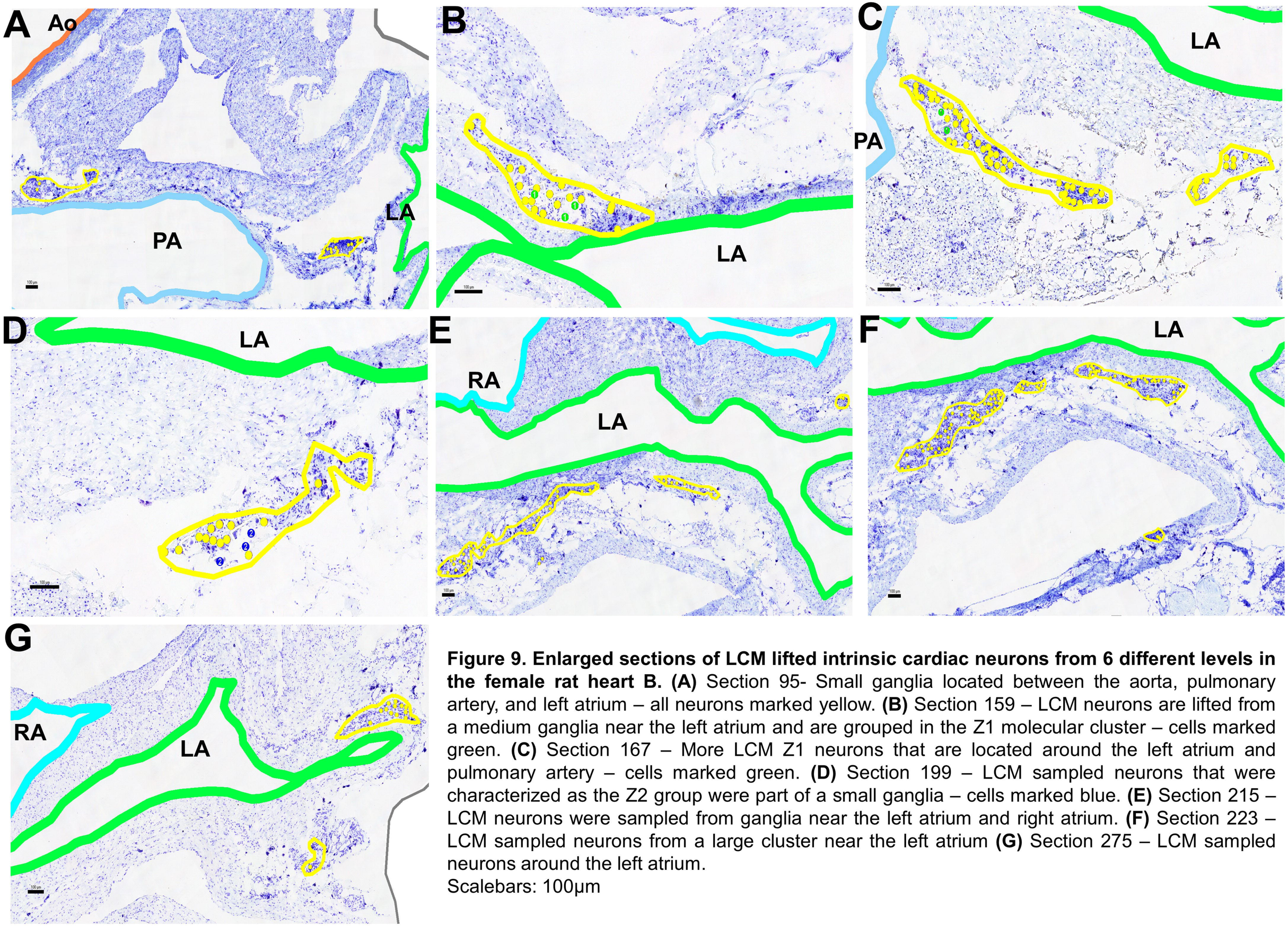

Figure 9. Enlarged sections of LCM lifted intrinsic cardiac neurons from 6 different levels in the female rat heart B. (A) Section 95- Small ganglia located between the aorta, pulmonary artery, and left atrium – all neurons marked yellow. **(B)** Section 159 – LCM neurons are lifted from a medium ganglia near the left atrium and are grouped in the Z1 molecular cluster – cells marked green. **(C)** Section 167 – More LCM Z1 neurons that are located around the left atrium and pulmonary artery – cells marked green. **(D)** Section 199 – LCM sampled neurons that were characterized as the Z2 group were part of a small ganglia – cells marked blue. **(E)** Section 215 – LCM neurons were sampled from ganglia near the left atrium and right atrium. **(F)** Section 223 – LCM sampled neurons from a large cluster near the left atrium **(G)** Section 275 – LCM sampled neurons around the left atrium.
Scalebars: 100μm

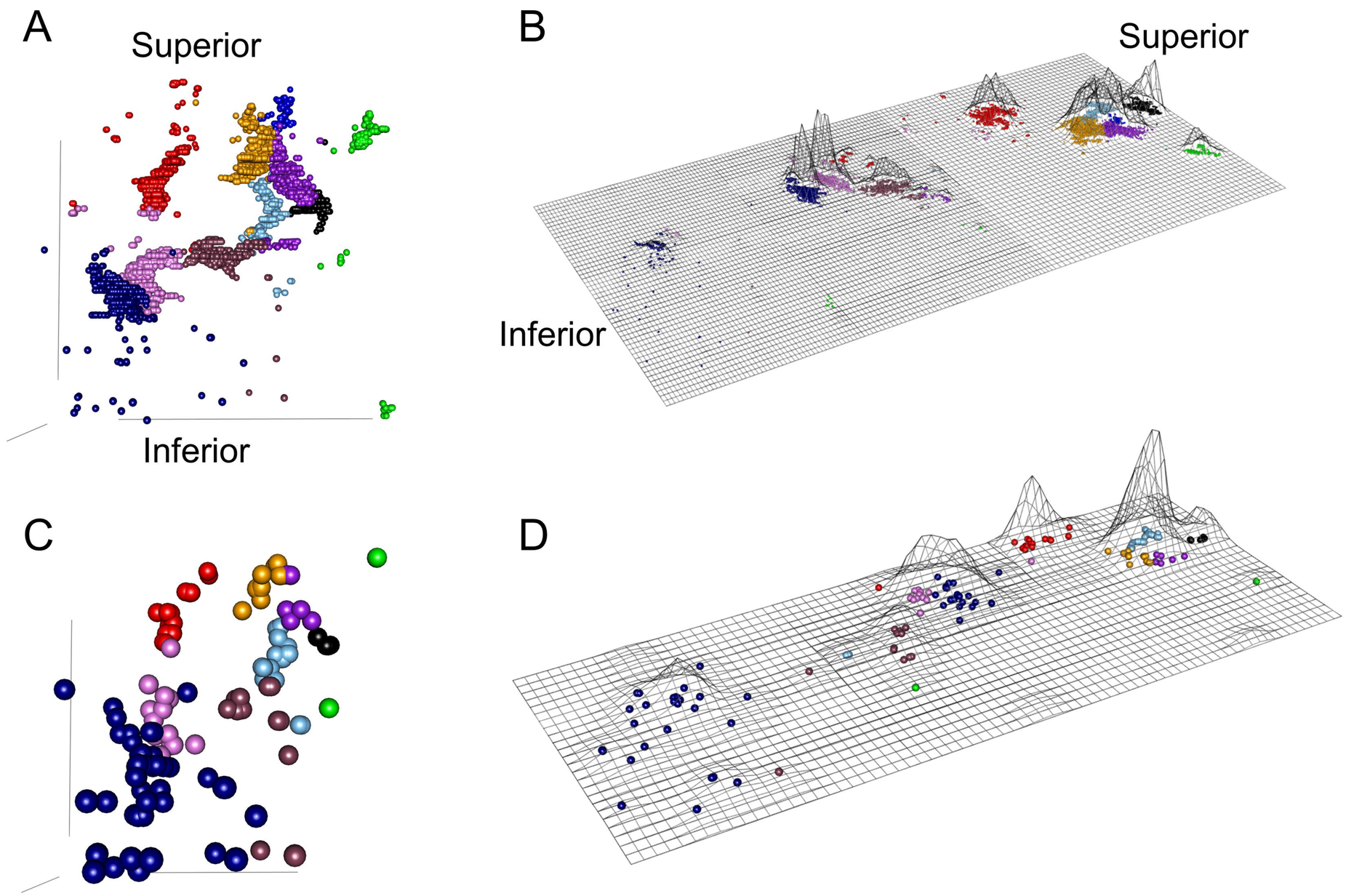

Figure 10. Identification of neuronal clusters in the Rat Heart—Heart B. Visualization of mapped neurons **(A)** and sampled neurons **(C)** in their 3D orientation. Flat-mount projection of mapped neurons **(B)** and sampled neurons **(D)** where the height of the contours are proportional to the density of neurons. 10 clusters of neurons were identified using the partitioning around medoids (PAM) algorithm, where identified clusters are shown in different colors.

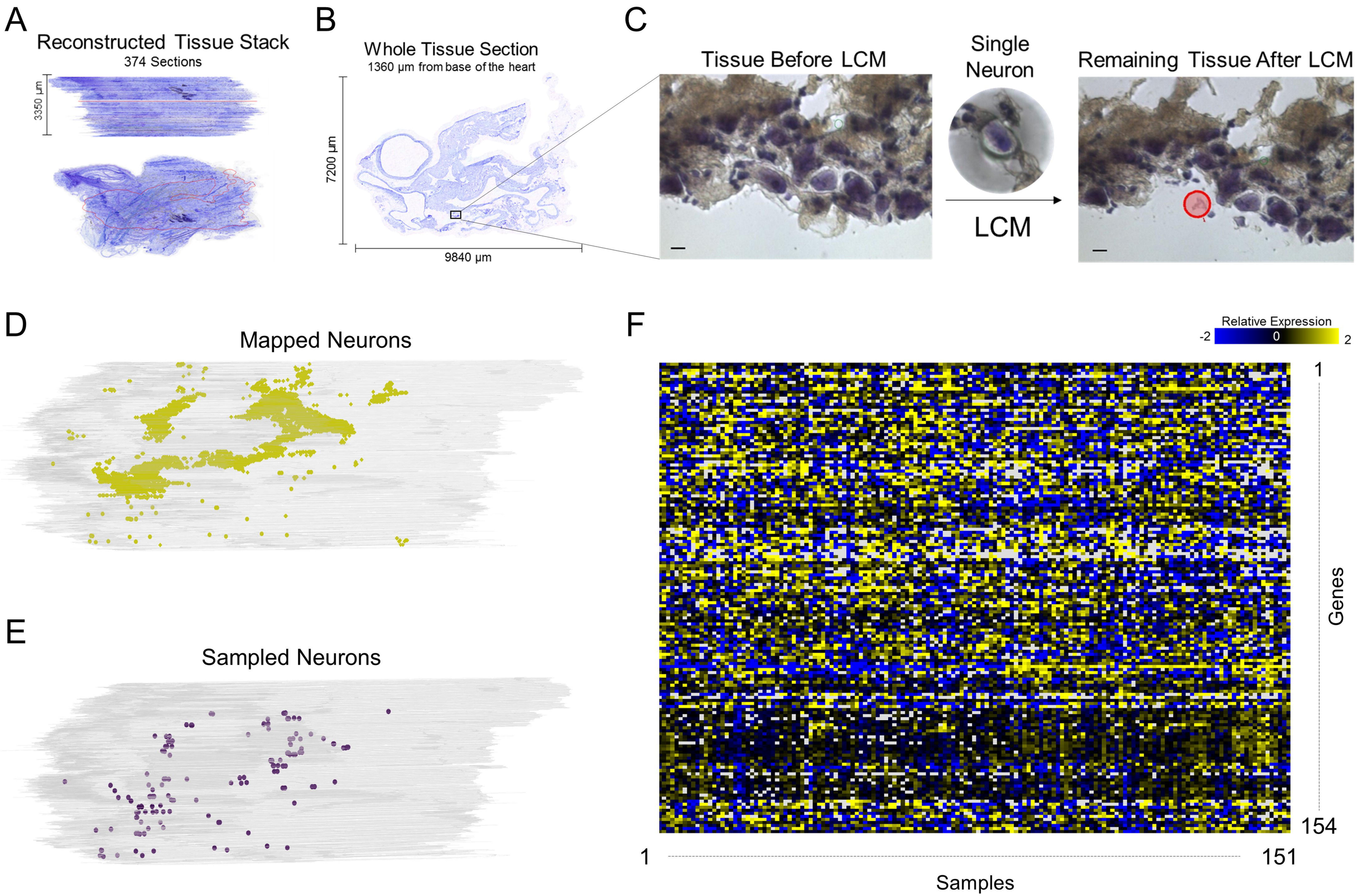
A
Reconstructed Tissue Stack
374 Sections
3350 µm
B
Whole Tissue Section
1360 µm from base of the heart
7200 µm
9840 µm
C
Tissue Before LCM
Single Neuron
LCM
Remaining Tissue After LCM
D
Mapped Neurons
E
Sampled Neurons
F
Relative Expression
-2
0
2
1
Genes
154
1
151
Samples

(Slide above)

Figure 11. Process of collecting and mapping Neurons from the rat heart. **(A)** A rat heart was sectioned at 20 um, imaged, and put into a 3D stack in TissueMaker. The red outline shows a specific section shown in (B). **(C)** the selected region from **(B)** is shown in a magnified view before and after laser capture microdissection, where the single neuron that has been collected can be seen on the LCM cap (middle). Distribution of mapped neurons **(D)** and sampled neurons **(E)** in the context of their 3D location as seen in TissueMapper. **(F)** Normalized qRT-PCR data showing expression of 154 genes for the 151 samples collected.

(Slide Below)

Figure 12. (A – B) Principal component analysis (PCA) plot of the 151 collected samples (A) show distinct separation according to their position along the Z axis of the heart (B). Samples were divided into three groups along the Z axis spanning from Z1 at the base of the heart to Z3 towards the apex. **(C)** Pavlidis template matching using Pearson correlation with a cutoff of 0.01 was used to find genes that show specific enrichment in one or more Z groups. A cutoff of 0.001 was used to find genes enriched in both the Z2 and Z3 group to increase specificity. **(D)** Expression of tyrosine hydroxylase (Th) vs. neuropeptide Y (Npy) (left) and Galanin (Gal) (right). **(E)** Expression of neuropeptide FF (Npff) vs. Cxcr4 (left) and Dbh (right). **(F)** 3D position of collected samples colored for expression of Th, Npff, and Cxcr4. While Th (F, left) and Npy (D, left) show little correlation between expression level and spatial location, Galanin (D, right) appears to be upregulated in the Z1 group. Npff (F, middle and E, left) shows downregulation in the Z2 group and distinct upregulation in the Z3 group. Cxcr4 (F, right and E, left) shows very high correlation between expression level and spatial location where expression is significantly downregulated in the Z1 group and significantly upregulated in the Z2 and Z3 groups. Dbh (E, right) shows mixed expression in the Z1 and Z2 groups with low expression in the Z3 group. It can also be seen that Npff and Dbh are anticorrelated in the Z3 group. For all panels, Z1 is represented in green, Z2 in blue, and Z3 in red.

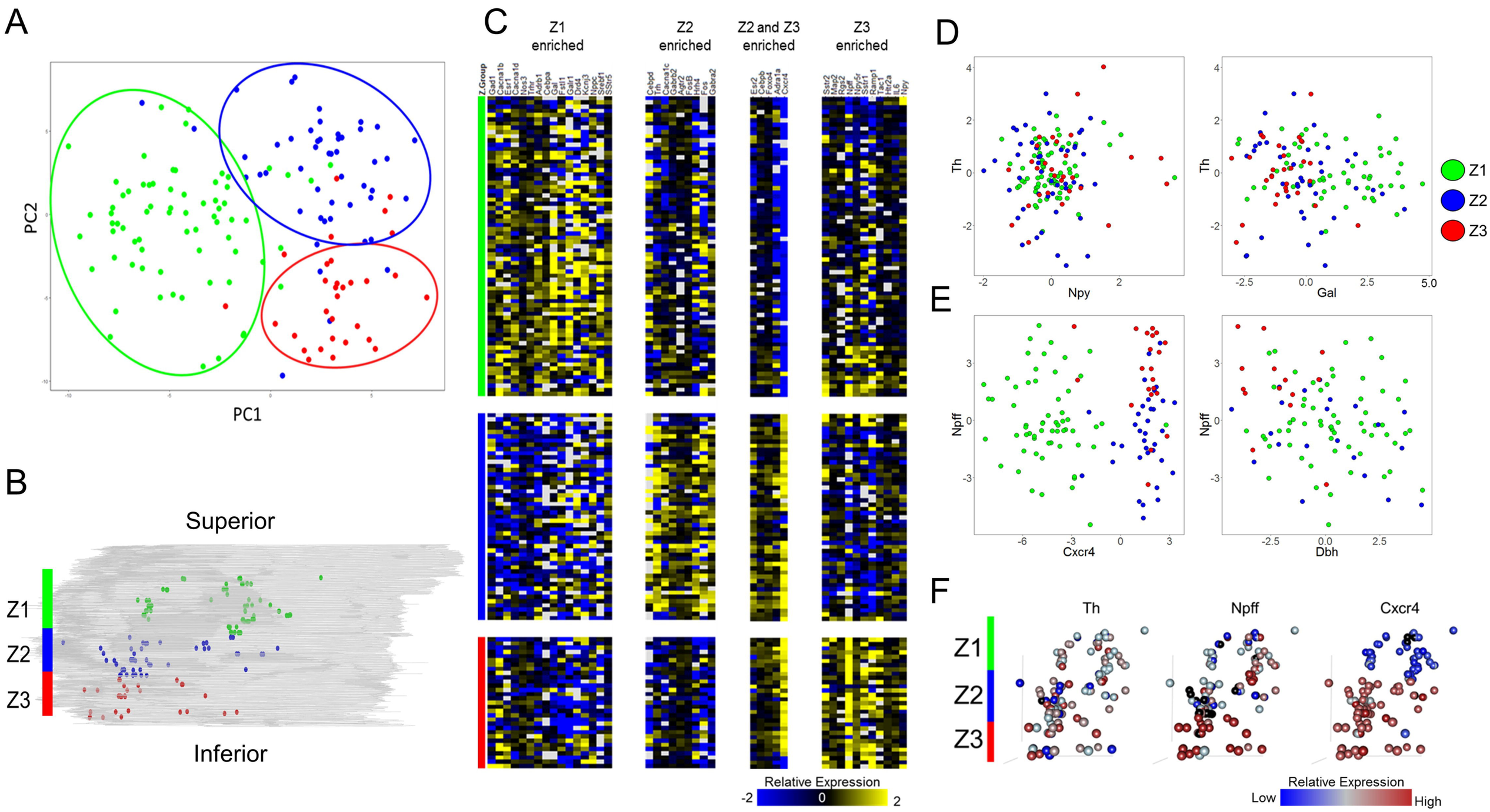
A
PC2
PC1
B
Superior
Z1
Z2
Z3
Inferior
C
Z1 enriched
Z2 enriched
Z2 and Z3 enriched
Z3 enriched
Z.Group
Gad1
Cacna1b
Esr1
Cacna1d
Nos3
Trhr
Adrb1
Cebpa
Gal
Fstl1
Galr1
Drd4
Kcnj3
Nppc
Sreb1
SStr5
Cebpd
Tfh
Cacna1c
Cacna2
Agtr2
FosB
Hrh4
Fos
Gabra2
Esr2
Cebpb
Foxo4
Adra1a
Cxcr4
Sstr2
Map2
Rgs2
Npff
Npy5r
Sstr1
Ramp1
Tac1
Htr2a
IL6
Npy
Relative Expression
-2
0
2
D
Th
Npy
Gal
Z1
Z2
Z3
E
Npff
Cxcr4
Dbh
F
Th
Npff
Cxcr4
Z1
Z2
Z3
Relative Expression
Low
High

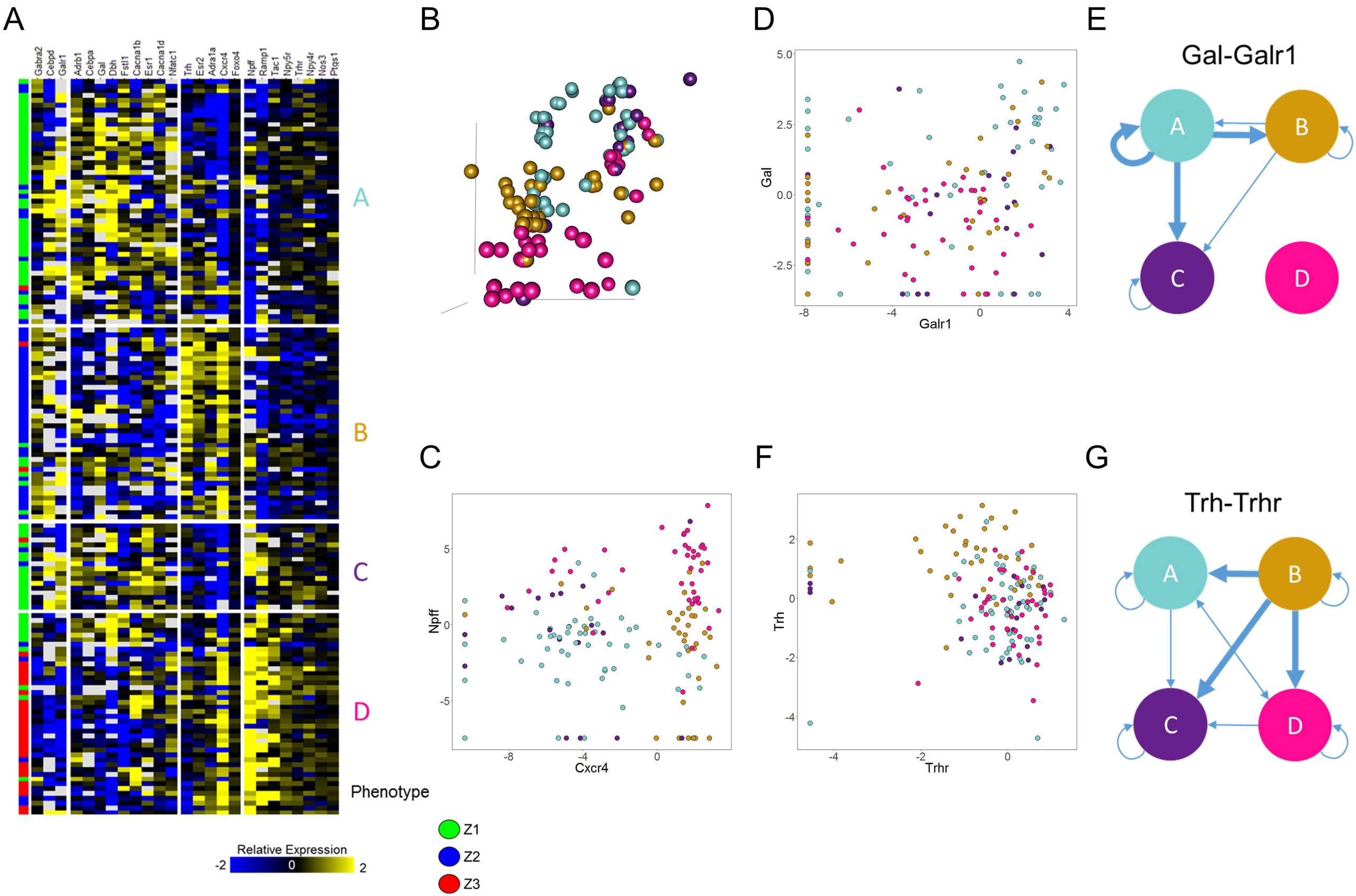
A
Gabra2
Cebpd
Galr1
Adrb1
Cebpa
Gal
Dbh
Fstl1
Cacna1b
Esr1
Cacna1d
Nfatc1
Trh
Esr2
Adra1a
Cxcr4
Foxo4
Npff
Ramp1
Tac1
Npy5r
Trhr
Npy4r
Nos3
Ptgs1
A
B
C
D
Phenotype
Relative Expression
-2
0
2
Z1
Z2
Z3
B
C
Npff
Cxcr4
D
Gal
Galr1
F
Trh
Trhr
E
Gal-Galr1
A
B
C
D
G
Trh-Trhr
A
B
C
D

Figure 13. Neuronal Phenotypes contributing to Spatial Separation. **(A)** ANOVA was performed with a threshold of 0.001 to find genes that contribute to the separation seen between the three Z groups. Selected genes were clustered using pearson correlation, resulting in the heatmap shown and giving rise to four different neuronal phenotypes (Labeled A-D). We can see that the Z1 group was split into phenotypes A and C, with some samples from the Z1 group clustering along with the Z3 group in phenotype D. Phenotype B is comprised mostly of samples residing in the Z2 group. **(B)** 3D position of collected samples, colored by phenotype. **(C)** Expression of Npff vs. Cxcr4, colored for phenotype. We can see that the comparison of these two genes largely determines the phenotypes. Phenotype A comprises mostly of cells that have low expression of Npff and Cxcr4. Phenotype B comprises mostly of cells that have low expression of Npff and high expression of Cxcr4. Phenotype C comprises largely of cells that have high expression of Npff and low expression of Cxcr4. Phenotype D comprises largely of cells that have high expression of both Npff and Cxcr4. **(D)** Expression of Galanin vs. its receptor Galr1 and **(E)** network diagram of putative galanin-mediated connectivity between neuronal phenotypes. **(F)** Expression of thyrotropin releasing hormone (Trh) and its receptor Trhr and **(G)** network diagram of putative Trh-mediated connectivity between neuronal phenotypes.